Chemical Science

ROYAL SOCIETY OF CHEMISTRY

EDGE ARTICLE

View Article Online
View Journal | View Issue

Cite this: *Chem. Sci.*, 2024, **15**, 17900

All publication charges for this article have been paid for by the Royal Society of Chemistry

Received 19th August 2024
Accepted 30th September 2024

DOI: 10.1039/d4sc05547k

rsc.li/chemical-science

Regulating Co–O covalency to manipulate mechanistic transformation for enhancing activity/durability in acidic water oxidation†

Jiachen Zhang,[a] Guangbo Chen,[bc] Dongmei Sun,[a] Yawen Tang,[a] Wei Xing,[de] Hanjun Sun *[a] and Xinliang Feng *[bf]

Developing earth-abundant electrocatalysts with high activity and durability for acidic oxygen evolution reaction is essential for H_2 production, yet it remains greatly challenging. Here, guided by theoretical calculations, the challenge of overcoming the balance between catalytic activity and dynamic durability for acidic OER in Co_3O_4 was effectively addressed *via* the preferential substitution of Ru for the Co^{2+} (T_d) site of Co_3O_4. *In situ* characterization and DFT calculations show that the enhanced Co–O covalency after the introduction of Ru SAs facilitates the generation of OH* species and mitigates the unstable structure transformation *via* direct O–O coupling. The designed Ru SAs-CoO_x catalyst (5.16 wt% Ru) exhibits enhanced OER activity (188 mV overpotential at 10 mA cm^{-2}) and durability, outperforming most reported Co_3O_4-based and Ru-based electrocatalysts in acidic media.

Introduction

Electrocatalytic water splitting is considered a promising approach for producing clean and renewable hydrogen owing to its high energy conversion efficiency and safety.[1–7] To date, acidic water electrolyzers exhibit great advantages compared with conventional alkaline water electrolyzers, such as lower ohmic losses, higher voltage efficiency and faster system response.[8–10] More importantly, the smaller gas crossover in acidic electrolyzers avoids the mixture of H_2 and O_2, which ensures higher gas purity (note S1†).[11,12] The acidic oxygen evolution reaction (OER) as the key half-reaction contributes to a major energy loss in overall electrochemical water splitting, which limits the efficiency of the overall process. Compared to the alkaline OER, acidic OER exhibits inferior catalytic activity due to the following two reasons: (1) the oxidation of adsorbed hydroxyl (OH*) into O_2 remains challenging in acidic media due to the scarcity of hydroxide anions (OH^-), resulting in lower OH* coverage on the catalyst surface. (2) The inferior durability of earth-abundant electrocatalysts (*e.g.*, Fe, Co, and Ni-based) in acidic electrolytes compared to that in alkaline electrolytes hinders their practical application.

To achieve efficient acidic water splitting, various catalysts with noble metal iridium (Ir) or ruthenium (Ru) as active sites have been widely studied, such as pyrochlore-type material $Y_2Ru_2O_{7-\delta}$,[13] bimetal oxide material (Li_xRuO_2 and[14] $Cr_{0.6}Ru_{0.4}O_2$,[15]), and perovskite-like material ($SrTi_{1-x}Ir_xO_3$ and[16] $Sr_2MIr(v)O_6$ [17]). However, the high cost and scarcity of noble metals limit their large-scale applications. Cobalt oxide (Co_3O_4) as an earth-abundant material has been theoretically predicted as a potential catalyst for the OER due to (1) the optimum binding energy with the O-intermediates, which is comparable to that of RuO_2;[18] (2) remarkable static durability (resting state or open-circuit potential) in acidic media owing to the relatively strong overlapping of the octahedral $Co^{3+}(O_h)$–O orbital.[19] However, its practical catalytic performance in acidic media is not satisfactory: (1) compared that in alkaline media with abundant OH^-, the OH* coverage on the catalyst surface in acidic media is comparatively lower; (2) in the conventional adsorbate evolution mechanism (AEM) process, the multiple processes preceding the formation of the O–O bond result in frequent valence changes, which facilitate surface reconstruction and limit the durability (Fig. S1a,† step 1–3).[20–22] Thereby, to enhance the activity and durability of Co_3O_4 for acidic OER, the local bonding environment is considered to be regulated to

[a]*Jiangsu Key Laboratory of New Power Batteries, Jiangsu Collaborative Innovation Center of Biomedical Functional Materials, School of Chemistry and Materials Science, Nanjing Normal University, 210023 Nanjing, China. E-mail: hanjun.sun@njnu.edu.cn*

[b]*Center for Advancing Electronics Dresden (CFAED) and Faculty of Chemistry and Food Chemistry, Technische Universität Dresden, 01062 Dresden, Germany. E-mail: xinliang.feng@tu-dresden.de*

[c]*Key Laboratory of Photochemical Conversion and Optoelectronic Materials, Technical Institute of Physics and Chemistry, Chinese Academy of Sciences, 100190 Beijing, China*

[d]*State Key Laboratory of Electroanalytic Chemistry, Jilin Province Key Laboratory of Low Carbon Chemistry Power, Changchun Institute of Applied Chemistry, Chinese Academy of Sciences, 130022 Changchun, China*

[e]*School of Applied Chemistry and Engineering, University of Science and Technology of China, 230026 Hefei, China*

[f]*Max Planck Institute of Microstructure Physics, Halle (Saale) 06120, Germany*

† Electronic supplementary information (ESI) available. See DOI: https://doi.org/10.1039/d4sc05547k

optimize the reaction process. With these considerations, a second adsorption site (lattice oxygen) is utilized to promote the direct O–O coupling during the OER process, namely the lattice oxygen oxidation mechanism (LOM). Direct O–O coupling not only mitigates the unstable reconstruction process before the formation of the O–O bond (Fig. S1b†), but also has the potential to surpass the theoretical limitation of activity in the conventional AEM.[23–26]

In order to facilitate the reaction pathway for direct O–O coupling, the moderate orbital overlap of metal–oxygen (M–O covalency) is essential.[24,27,28] Specifically, the enhanced M–O covalency results in a decreased energy gap between the metal d and O 2p band center, thereby moving the Fermi level closer to the O 2p-band center and the redox potential of the O_2/H_2O couple, which is thermodynamically favorable for the redox of lattice oxygen.[29,30] Nevertheless, excessive covalency would cause an improved lattice oxygen migration rate compared to the vacancy filling rate during the LOM cycles, leading to structure destabilization.[5,31] Therefore, we propose that moderate Co–O covalency of Co_3O_4 is more advantageous for enhancing durability compared to the AEM process by mitigating the unstable reconstruction process. In the present study, guided by the theoretical calculations, we design an electrocatalyst composed of Ru single atom (5.16 wt%) doped cobalt oxide (Ru SAs-CoO_x) to overcome the activity/durability tradeoff for acidic OER. Our theoretical calculations suggest that (1) the introduction of heteroatom Ru could benefit the generation of OH* species, thus providing plentiful OH* species for the subsequent oxidation process;[25] (2) the introduction of Ru allows the enhanced orbital overlap between the Co 3d and O 2p, thus increasing the Co–O covalency;[28] (3) the doping of Ru promotes the generation of oxygen vacancies (O_v), facilitating direct O–O coupling during the OER process and the oxygen evolution from lattice oxygen.[19,32,33] *In situ* ^{18}O isotope labeling differential electrochemical mass spectrometry (DEMS) demonstrated Ru to be the switch promoting oxygen evolution from lattice oxygen. In addition, *in situ* Raman spectroscopy suggested that the growth of stable amorphous cobalt oxide on the electrode surface acted as the protective layer enhancing the durability. As a result, the prepared Ru SAs-CoO_x catalyst delivers a low overpotential of 188 mV at a current density of 10 mA cm^{-2}, and enhanced long-term durability in acidic media, which are superior to those of pristine Co_3O_4 (395 mV at 10 mA cm^{-2}) and commercial RuO_2 (312 mV at 10 mA cm^{-2}).

Results and discussion

Theoretical prediction for the structure of the electrocatalyst

Density functional theory (DFT) calculations were first performed to investigate the participation of the lattice oxygen oxidation reaction of Ru SAs-CoO_x. To ascertain the doping position of Ru, we compared the formation energy for the substitution of tetrahedral Co^{2+} (T_d) and octahedral Co^{3+} (O_h) sites for a single Ru atom, which could effectively explore the influence of the doping element on the local reaction environment. As displayed in Fig. S2–S3,† replacing Co^{2+} (T_d) with Ru leads to a lower barrier (1.194 eV) compared to that of the Co^{3+} (O_h) site (2.803 eV), indicating a thermodynamically preferred replacement of Ru atoms at the Co^{2+} (T_d) site. Then, to evaluate the feasibility of the lattice oxygen oxidation reaction after Ru doping, the Co–O covalency and O_v formation energy of Co_3O_4 and Ru–Co_3O_4 are calculated, respectively. As illustrated in Fig. 1a–c and Table S1,† the substitution of divalent tetrahedral Co^{2+} (T_d) with Ru^{3+} reduces the localized gap between the Co 3d and O 2p band center, accompanied by an increased orbital overlap between Co 3d and O 2p. Therefore, the antibonding states below the Fermi level displayed a higher oxygen character that results in the enhanced Co–O covalency, which would thermodynamically promote the oxidation of lattice oxygen.[34,35]

Besides, considering the crucial role of O_v formation in facilitating direct O–O coupling, the O_v formation energy in Co_3O_4 and Ru–Co_3O_4 is also calculated. The formation energies of four different types of O_v in Co_3O_4 are 1.509, 0.450, 2.863, and 2.820 eV, respectively (Fig. S4†). In the case of Ru–Co_3O_4, the corresponding formation energies for these four types of O_v are 0.149, 0.362, 1.676, and 1.362 eV (Fig. S5†). It is clear that the substitution of Co with Ru significantly reduces the formation energy of O_v. Therefore, the increased Co–O covalency and the lower O_v formation energy facilitate the transformation of the OER mechanism from a conventional adsorbate evolution mechanism (AEM, OH attack) to a lattice oxygen oxidation mechanism (LOM, O–O coupling) (Fig. 1d).[32,33] In addition, it is worth noting that it is difficult to carry out accurate DFT studies to represent the exact surface of the electrocatalyst and the local experimental conditions. However, DFT calculations here may provide side insight for the design of electrocatalysts and lateral understanding of the structural and catalytic mechanism changes after the incorporation of Ru.

Material synthesis and characterization

Guided by the theoretical prediction results, we synthesized Ru SAs-CoO_x by a cation exchange method. The detailed synthetic procedure and structural changes are illustrated in Fig. S6† and 2a. First, a cobalt precursor (Co-pre) with "flower-like" morphology (Fig. S7 and S8a–b†) was prepared *via* co-precipitation of $Co(CH_3COO)_2 \cdot 4H_2O$ and polyvinylpyrrolidone (PVP) in ethylene glycol under the protection of argon at 170 °C. Herein, PVP was employed to improve the uniformity of the final architecture. Next, the prepared Co-pre was annealed at 300 °C to yield the pristine Co_3O_4 nanoflower (Fig. S8c–d†). Subsequently, the Co_3O_4 nanoflower (10 mg) was added into the ruthenium chloride (0.075 mmol) solution and stirred at 60 °C for the cation exchange reaction (5.16 wt% Ru). Finally, the Ru SAs-CoO_x sample was obtained after calcination at 300 °C, which could detach the chloride ligands and improve crystallization.[36,37]

X-ray diffraction (XRD) was employed to investigate the crystal structure of Co_3O_4 and Ru SAs-CoO_x. As depicted in Fig. 2b–c, the diffraction peaks of Co_3O_4 were exhibited in the XRD pattern of Ru SAs-CoO_x, and no diffraction peaks corresponding to Ru-related species could be detected, suggesting that the Ru species were highly dispersed or amorphous.[38] However, the incorporation of Ru^{3+} with a larger ionic radius

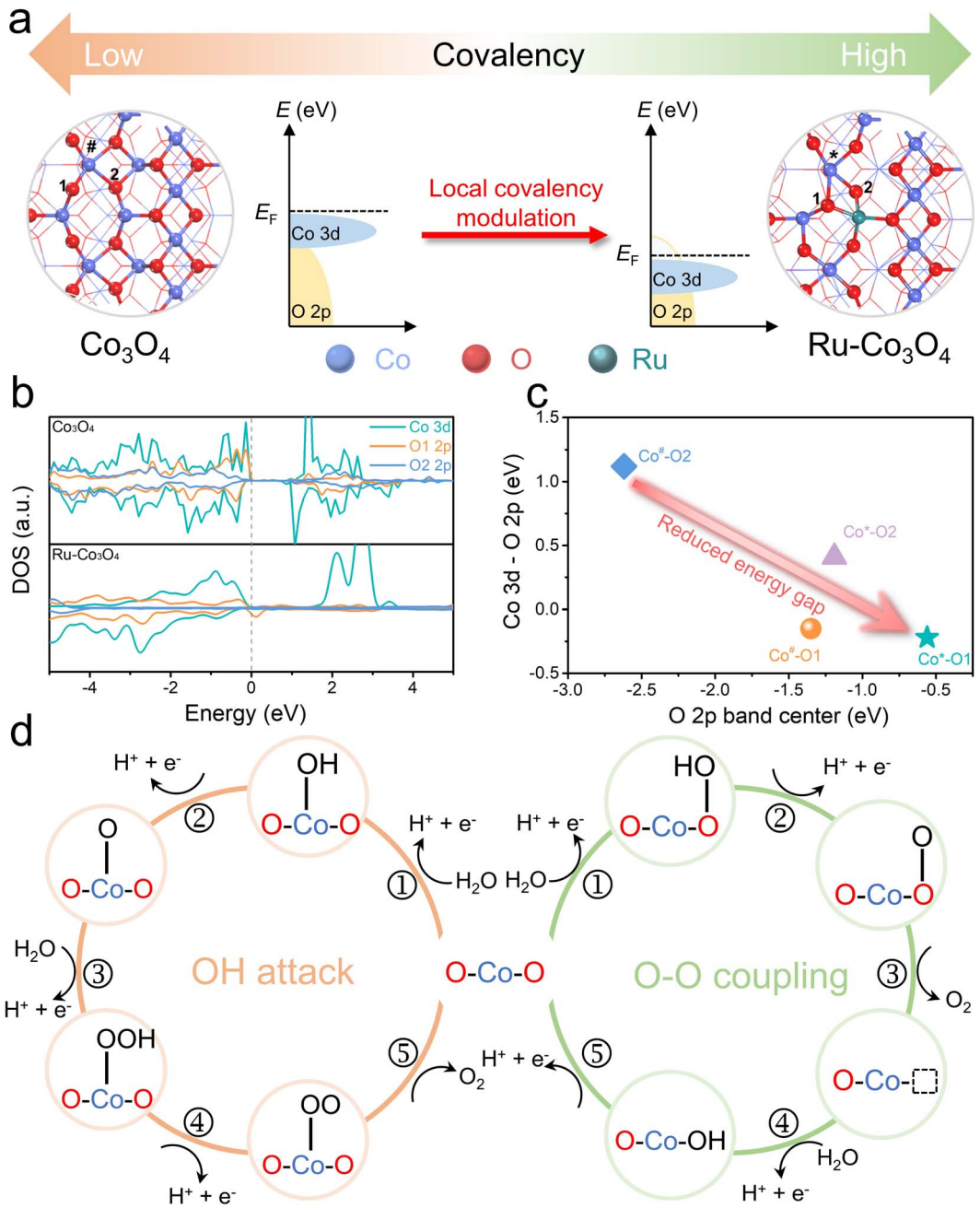

Fig. 1 Electronic structures and OER pathways. (a) Structures and schematic energy bands of Co_3O_4 and Ru–Co_3O_4 (the corresponding structure is shown in Fig. S5a†). (b) Computed DOS of Co 3d and O 2p for Co_3O_4 and Ru–Co_3O_4. (c) Energy gap between Co 3d and O 2p *versus* the O 2p band center for Co_3O_4 and Ru–Co_3O_4. (d) Proposed transformation of the OER mechanism from the AEM to LOM after the doping of Ru.

resulted in an increase in micro-strain within the Co_3O_4 lattice. Consequently, Ru SAs-CoO_x displayed a clear XRD peak width broadening (~0.3°), as well as a negative diffraction peak shift (~0.2°) compared to pristine Co_3O_4, which confirmed that the incorporation of Ru is not limited to the surface but extends into the Co_3O_4 framework.[38,39] Besides, the broad peak observed between 20° and 30° can be attributed to the presence of carbon residue primarily derived from ethylene glycol and $Co(CH_3COO)_2$. The morphologies of Ru SAs-CoO_x were then examined using transmission electron microscopy (TEM). As shown in Fig. 2d and S9–S10,† after introducing Ru atoms, Co_3O_4 was transformed into the disordered nanosheet structure, where the interconnected nanostructures with certain amounts of holes could be observed. The N_2 adsorption–desorption isotherms and the corresponding Brunauer–Emmett–Teller (BET) analysis showed that the surface area of Ru SAs-CoO_x (155.46 $m^2\ g^{-1}$) was higher than that of pristine Co_3O_4 (33.73 $m^2\ g^{-1}$), while the average pore size of Ru SAs-CoO_x (4.41 nm) was found to be

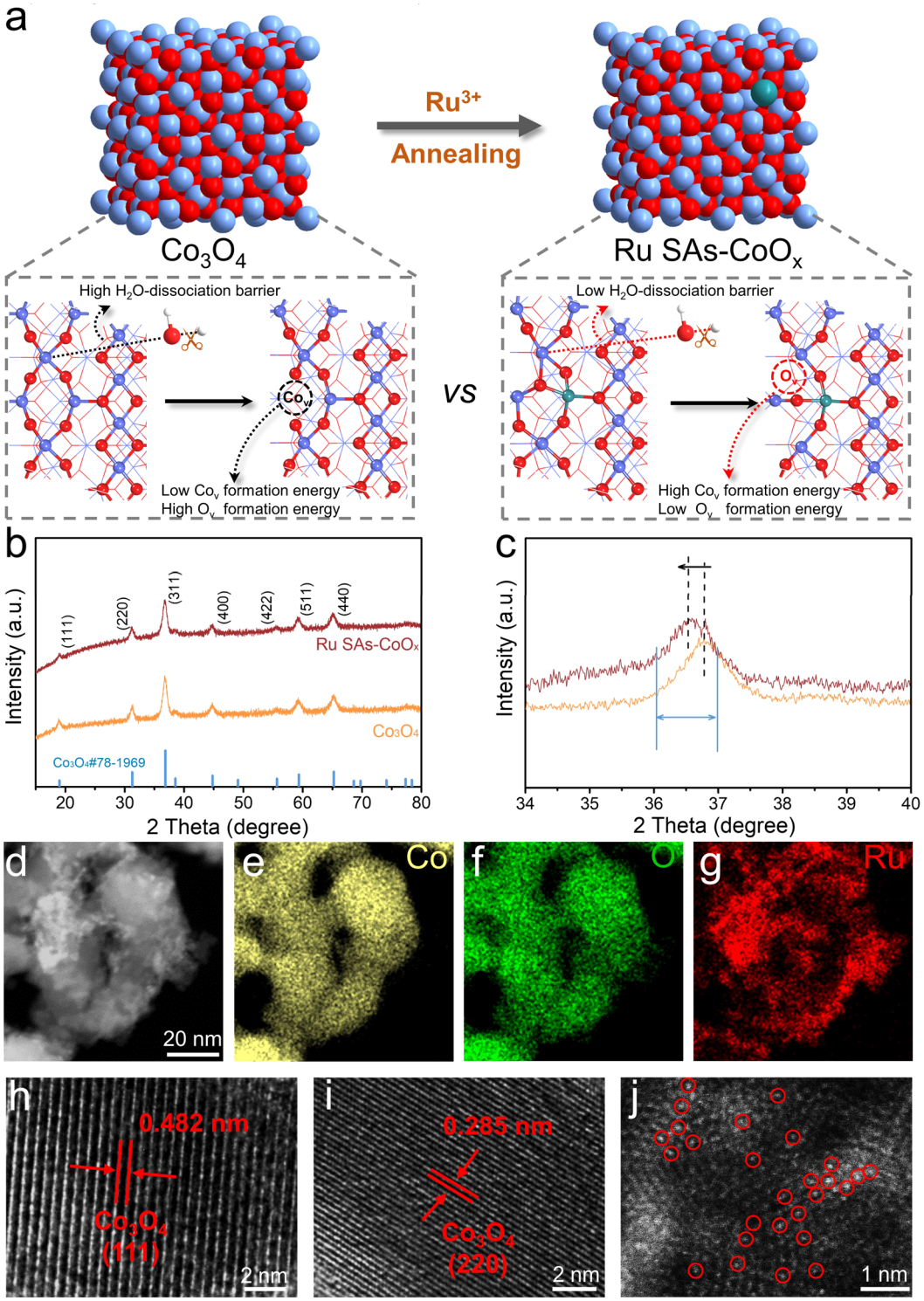

Fig. 2 Schematic illustration of the synthesis, mechanism, and morphological characterization studies. (a) The synthetic procedure and mechanism of Ru SAs-CoO_x as an efficient electrocatalyst for acidic OER. (b) XRD patterns of Ru SAs-CoO_x and Co_3O_4 (*ca.* 3° min^{-1}). (c) Enlarged XRD pattern of Ru SAs-CoO_x and Co_3O_4. (d–g) HAADF-STEM images of Ru SAs-CoO_x and the corresponding elemental mapping images of Co, O, and Ru. (h and i) HRTEM images of Ru SAs-CoO_x. (j) Atomic-resolution HAADF-STEM image of Ru SAs-CoO_x, Ru atoms (marked by red circles) are uniformly distributed on the surface of CoO_x.

smaller compared with that of pristine Co_3O_4 (13.27 nm) (Fig. S11†). The above-mentioned results were attributed to the "etching-recombination" that occurred during the cation exchange process, which led to an increased surface area, and exposed more sites for the electrocatalysis of the OER. In addition, the elemental mapping images indicated the uniform

distribution of Ru, Co, and O atoms in the selected porous nanosheets, confirming the successful introduction of Ru after the cation exchange process (Fig. 2e–g). More structural features of Ru SAs-CoO_x were then explored by high-resolution transmission electron microscopy (HRTEM). Two obvious continuous and ordered lattice fringes with lattice spacings of 0.482 and 0.285 nm were observed, which corresponded to the (111) and (220) planes of Co_3O_4 (Fig. 2h–i). No lattice fringes derived from Ru nanoparticles could be found. From the high-angle annular dark-field scanning transmission electron microscopy (HAADF-STEM) images, numerous atomically dispersed bright dots (highlighted with red circles) of Ru atoms were homogeneously distributed on the surface of Ru SAs-CoO_x, confirming that Ru species were anchored on Co_3O_4 in the form of single-atoms during the cation exchange process (Fig. 2j and S12†).[40–42]

Electron spin resonance (ESR) measurements were performed to investigate the generation of O_v, and the signal corresponding to the electron trapped on O_v was detected at $g = 2.003$. As shown in Fig. 3a, a stronger signal intensity of Ru SAs-CoO_x was exhibited relative to pristine Co_3O_4, demonstrating higher O_v concentration.[43] To further substantiate the association between the increase in O_v concentration and Ru doping, Ru-CoO_x catalysts with different Ru contents were prepared by varying the dosage of Ru^{3+} (*i.e.*, 0.025 mmol, 0.05 mmol, and 0.075 mmol). The resulting products were denoted as Ru-CoO_x-0.025, Ru-CoO_x-0.05, and Ru-CoO_x-0.075 (*i.e.* Ru SAs-CoO_x), respectively. The results of ESR also showed that the O_v concentration increased significantly with the enhancement of Ru content (from 0 to 5.16 wt% measured by ICP-AES) (Fig. S13†).

XPS spectra were also measured to elucidate the chemical compositions and valence state of the prepared electrocatalysts (Fig. S14–S15†). For the Co 2p spectrum of Ru SAs-CoO_x, two major peaks located at 779.3 and 794.7 eV were assigned to Co $2p_{3/2}$ and Co $2p_{1/2}$, which were fitted by two regions of Co^{2+} and Co^{3+}. The relative atomic ratio of Co^{2+}/Co^{3+} could be obtained by comparing the area of the fitted curve. As more oxygen vacancies were generated on the surface of Ru SAs-CoO_x, the ratio of Co^{2+}/Co^{3+} in Ru SAs-CoO_x was expected to increase.[44,45] However, the ratio of Co^{2+}/Co^{3+} for the O_v-rich Ru SAs-CoO_x

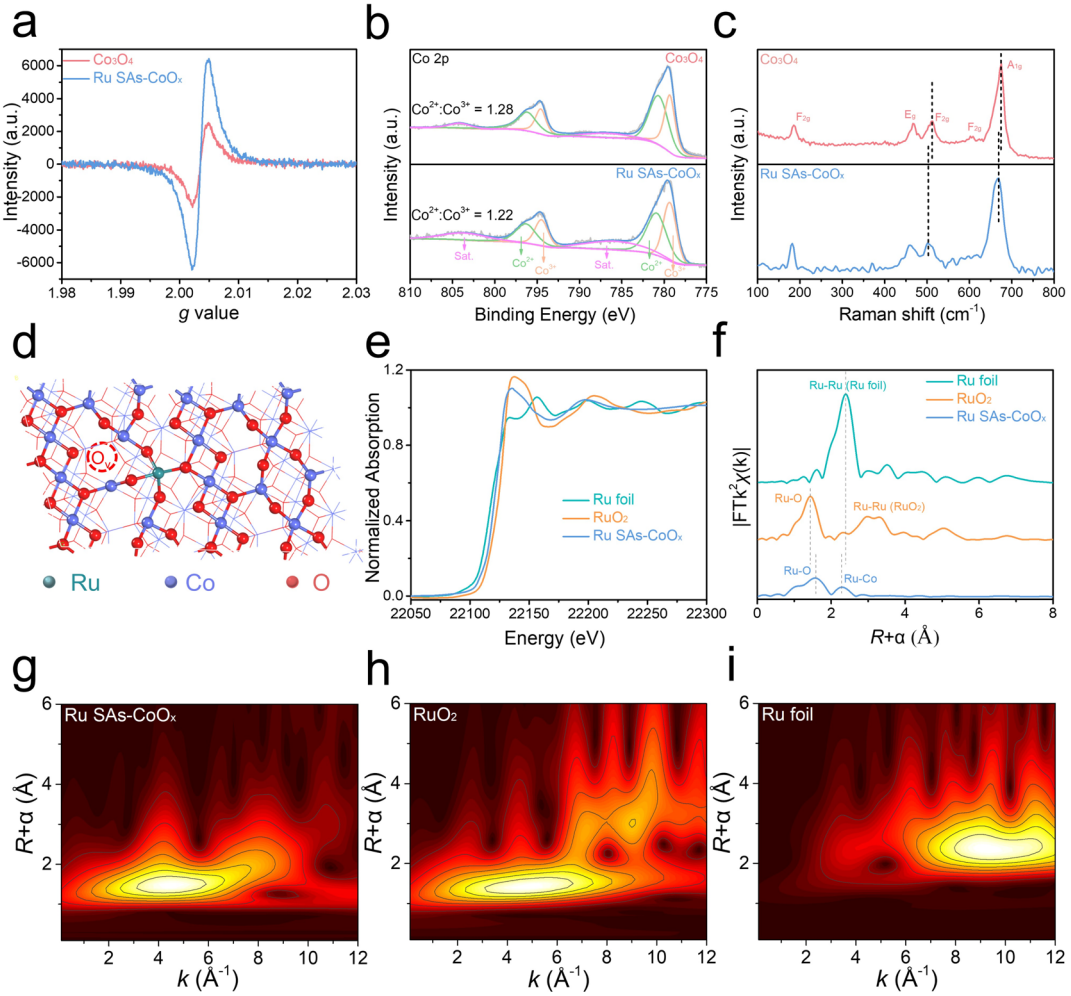

Fig. 3 Structure characterization of Ru SAs-CoO_x. (a) ESR spectra of Ru SAs-CoO_x and Co_3O_4. (b) Co 2p XPS spectra of Ru SAs-CoO_x and Co_3O_4. (c) Raman spectra of Ru SAs-CoO_x and Co_3O_4. (d) Structure of Ru SAs-CoO_x. (e) Ru *K*-edge XANES spectra of Ru SAs-CoO_x, Ru foil, and RuO_2. (f) Fourier-transformed Ru *K*-edge EXAFS spectrum of Ru SAs-CoO_x, Ru foil, and RuO_2. (g–i) Wavelet transforms for the k^2-weighted Ru *K*-edge EXAFS signals of Ru SAs-CoO_x, Ru foil, and RuO_2.

(1.22) showed a slight decrease compared to that of the pristine Co_3O_4 (1.28) (Fig. 3b), which indicated that the Ru atoms were doped into the Co_3O_4 framework to maintain electrical neutrality, rather than being adsorbed on the surface. In addition, the ratio of Co^{2+}/Co^{3+} for Ru SAs-CoO_x (1.22) showed a slight decrease compared to that of the pristine Co_3O_4 (1.28), which suggested that Ru preferentially occupied T_d sites (~78%, note S2†).[46,47] In the Ru 3p spectrum (Fig. S14d†), the peaks of Ru $3p_{3/2}$ and Ru $3p_{1/2}$ located at 462.60 and 484.88 eV were detected, which are positioned between those of Ru (0) and Ru (IV),[48] demonstrating that the oxidation state of Ru in Ru SAs-CoO_x was between 0 and +4 (Fig. S16†). Then Raman spectroscopy was conducted to reveal the structural changes in the coordination environment of Co_3O_4.[49] As shown in Fig. 3c, five characteristic peaks corresponding to the E_g, F_{2g}, and A_{1g} of Co_3O_4 were detected. Specifically, A_{1g} represented the octahedral (O_h) sites while F_{2g} corresponded to the tetrahedral (T_d) sites. After doping of Ru species, notable shifts in the characteristic peaks of F_{2g} (~11 cm^{-1}) and A_{1g} (~7 cm^{-1}) were observed, providing clear evidence of Ru substitution at both tetrahedral (T_d) and octahedral (O_h) sites. The larger shift for F_{2g} than that for A_{1g} suggests that the Ru preferentially occupied the T_d sites (Fig. 3d).[49] In order to investigate the local coordination of Ru species in Ru SAs-CoO_x, the Ru *K*-edge region X-ray absorption near edge structure (XANES) was measured, which displayed clear differences from those of Ru foil and RuO_2 (Fig. 3e). Extended X-ray absorption fine structure (EXAFS) for Ru SAs-CoO_x was performed to analyze the bonding forms of Ru species. The peak at 1.57 Å was associated with the back scatterings between Ru and neighboring O in Ru SAs-CoO_x. Another peak at 2.29 Å could be attributed to the back scatterings between metal and metal. Furthermore, quantitative EXAFS curve-fitting analyses for Ru SAs-CoO_x revealed that the average coordination number between Ru and O was 3.7 (Fig. S17 and Table S2†), which further demonstrates the preference of Ru substitution at the T_d site (a 4-coordination structure) over the O_h site (6-coordination structure). Additionally, the presence of O_v may contribute to a further decrease in the average coordination number. The wavelet transform (WT) analysis of the EXAFS spectrum was performed to further confirm the formation of Ru SAs (Fig. 3g–i). Only one intensity maximum at about 4.5 $Å^{-1}$ (Ru–O scattering path) was detected in the WT contour plot of Ru SAs-CoO_x. The signal corresponding to Ru_B–O–Co_B was not detected, which may be due to its weaker coordination.

Electrocatalytic performance of the OER in acidic media

The electrocatalytic performances of the prepared catalysts were evaluated with a three-electrode system at room temperature. The *iR*-corrected polarization curves recorded by linear scan voltammetry (LSV) in N_2-saturated 0.1 M $HClO_4$ electrolyte were displayed. When the content of Ru reached 5.16 wt% (Fig. S18–S24 and Tables S3 and S4†) in the obtained Ru-CoO_x (Ru SAs-CoO_x) catalyst, it showed a minimum overpotential of 188 mV at a current density of 10 mA cm^{-2}, which was much smaller than that of commercial RuO_2 (312 mV) and pristine Co_3O_4 (395 mV) (Fig. 4a). Then the Tafel slopes derived from the polarization curves were used to evaluate the catalytic kinetics. As shown in Fig. 4b, the Tafel slope of Ru SAs-CoO_x was calculated to be 63 mV dec^{-1}, which was much lower than that of pristine Co_3O_4 (111 mV dec^{-1}) and commercial RuO_2 (84 mV dec^{-1}), indicating the faster kinetics toward the OER.[50,51] The Tafel slopes of all samples fell within the range of 60–120 mV dec^{-1}, indicating a mixed kinetic control mechanism where the overall rate is not controlled by a single path.[20,52–54] Besides, several other points may also cause the value of the Tafel slope to deviate from 60 mV dec^{-1} or 120 mV dec^{-1}: (1) transfer coefficient (α) largely deviates from the commonly assumed value; (2) the coverage would vary as the electrode potential increases, leading to a corresponding alteration in the Tafel slope;[1] (3) the catalytic activity may originate from multiple active sites, limiting the application of the conventional Butler–Volmer formalism. The low overpotential and Tafel slope of Ru SAs-CoO_x also demonstrated its superior performance among Co_3O_4-based electrocatalysts, which is even well comparable with the reported Ir-based and Ru-based OER electrocatalysts in acidic media, such as Co–RuIr (235 mV at 10 mA cm^{-2}),[55] Ru@IrO_x (282 mV at 10 mA cm^{-2}),[56] amorphous IrO_2 (255 mV at 10 mA cm^{-2}),[57] Ba_2YIrO_6 (318 mV at 10 mA cm^{-2}),[58] Ir-STO (295 mV at 10 mA cm^{-2}),[59] and $RuNi_2$@G-250 (210 mV at 10 mA cm^{-2})[60] (Fig. 4c and Table S5†). In addition, the exchange current density (j_0) of Ru SAs- CoO_x (0.033 mA cm^{-2}) could be evaluated by extrapolating the Tafel slope (Fig. S25†), which was much higher than those of pristine Co_3O_4 (0.004 mA cm^{-2}) and commercial RuO_2 (0.012 mA cm^{-2}), demonstrating the fast electron transfer rate between the electrode and Ru SAs-CoO_x catalyst surface.

We further investigated the electrochemical surface area (ECSA) of Ru SAs-CoO_x by testing the double layer capacitances (C_{dl}). Compared with those of pristine Co_3O_4 (0.5 mF cm^{-2}) and RuO_2 (14.5 mF cm^{-2}), the larger C_{dl} value (18.6 mF cm^{-2}) suggested that more electrochemical surface area was generated (Fig. S26†). Considering that the changes in morphology would impact the activity, different elements (Mn, Fe, and Ni) were introduced to explore their morphologies and catalytic activity. As shown in Fig. S27–S29,† after the introduction of other different elements, the morphologies all transformed into the nanosheet structure. However, there was no observed enhancement in the catalytic activity. This could be attributed to the fact that compared to these 3d transition metals, Ru exhibited stronger capacity for H_2O dissociation, which benefited the generation of OH* species, thereby facilitating the generation of abundant OH* species and subsequently enhancing catalytic activity. Therefore, the introduction of Ru was primarily responsible for the observed enhancement in catalytic activity. Turnover frequencies (TOFs) as another important parameter could be applied to evaluate the intrinsic activity per site of the catalyst.13,44,61 Although many methods have been applied to estimate the number of active sites, accurate estimation of the TOF is still a challenge. Here, the lower limit TOF of the Ru SAs-CoO_x and RuO_2 electrodes was estimated by making an approximation that all metal centers in the catalysts are available for the OER.[62–64] As displayed in Fig. 4d, the lower limit TOF value of Ru SAs-CoO_x at 1.5 V is as high as 0.02 s^{-1}, 7.7 times higher than that of RuO_2. The

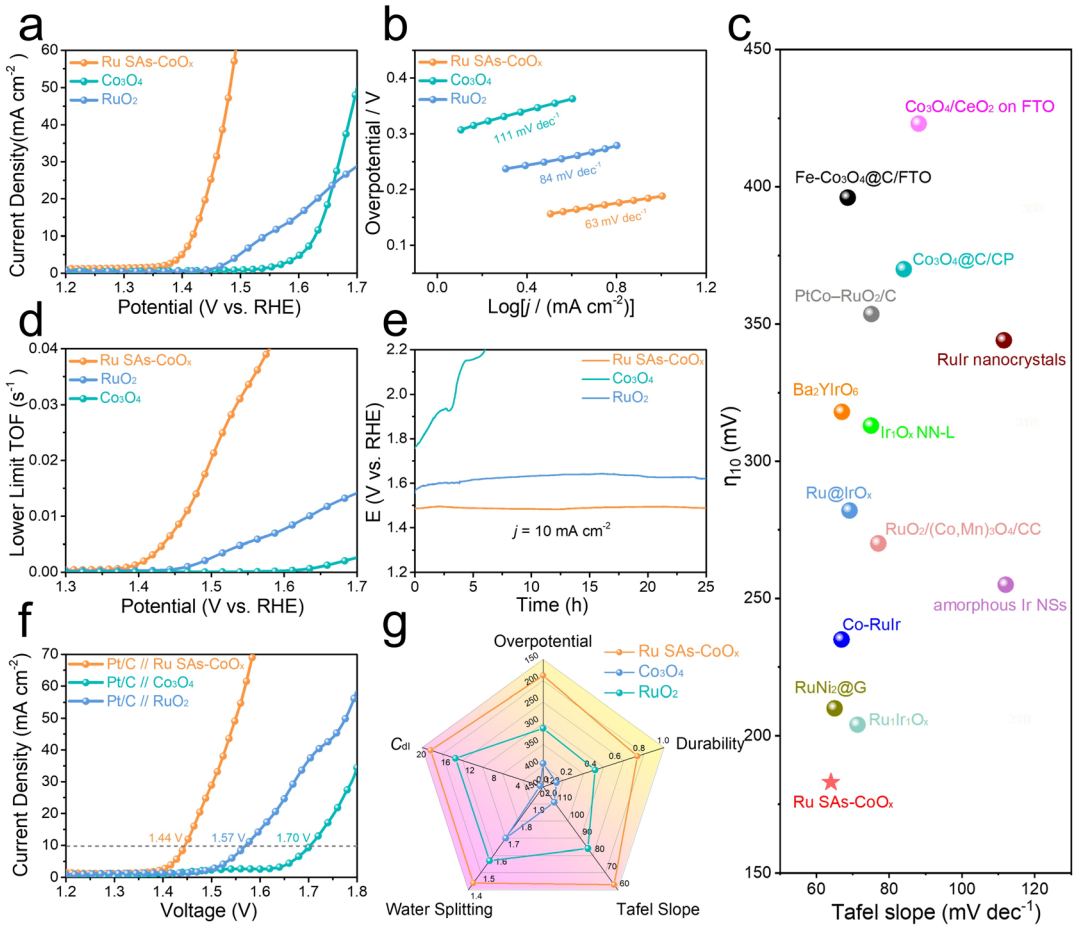

Fig. 4 Catalytic activity for the OER and overall water splitting. (a and b) OER polarization curves and corresponding Tafel slopes of Ru SAs-CoO_x, Co_3O_4, and RuO_2. (c) Comparison with the recently reported Ru-based, Ir-based, and Co-based OER electrocatalysts. (d) Lower limit TOF curves of Ru SAs-CoO_x, Co_3O_4, and RuO_2. (e) Chronopotentiometric curves of Ru SAs-CoO_x, Co_3O_4, and RuO_2 recorded at a constant current density of 10 mA cm^{-2}. (f) Polarization curves of the Pt/C//Ru SAs-CoO_x, Pt/C//Co_3O_4, and Pt/C//RuO_2 electrolyzers for overall water splitting. (g) Comparison of overpotential (mV @ 10 mA cm^{-2}), durability (current retention ratio), Tafel slope (mV dec^{-1}), water splitting (mV @ 10 mA cm^{-2}), and C_{dl} (mF cm^{-2}) for Ru SAs-CoO_x, Co_3O_4, and RuO_2.

faradaic efficiency of nearly 100% for the OER on Ru SAs-CoO_x was evaluated by the water drainage method, indicating excellent selectivity for oxygen generation (Fig. S30†).

Durability is an important parameter to evaluate the OER performance in acidic media. Chronopotentiometry tests were conducted at a current density of 10 mA cm^{-2}. As revealed in Fig. 4e, Ru SAs-CoO_x displayed a slight potential change from 1.485 to 1.494 V after 25 hours, which was far better than that of RuO_2 (1.556 V to 1.623 V, aligned with the trend of commercial RuO_2 in the reported literature studies.[6,9]) and pristine Co_3O_4. Meanwhile, the chronoamperometric curves of Ru SAs-CoO_x, RuO_2 and pristine Co_3O_4 were also recorded at the same initial current density (10 mA cm^{-2}). The results indicated that the current retention of Ru SAs-CoO_x after 20 hours was 77.3%, which was superior to RuO_2 (43.3%) and pristine Co_3O_4 (10.6%) (Fig. S31†). Meanwhile, the durability of Ru SAs-CoO_x was also compared with previously reported Co_3O_4 electrocatalysts, which also exhibited a significantly better durability (Table S6†). After the durability test, the morphology, electronic structure, and composition of the catalysts were studied. As displayed in Fig. S32–S34,† HRTEM and EDS results confirmed that the Ru SAs-CoO_x still maintained a porous structure and all the elements (Ru, Co and O) could be detected. Meanwhile, a slight positive shift was observed in Co 2p and O 1s spectra, confirming an increase in valence state at oxidative potentials. This shift can be attributed to the oxidative conditions during the OER process.[65,66] The XRD pattern revealed that the Co_3O_4 phase of Ru SAs-CoO_x was well-maintained, although the peak intensity decreased obviously. This decrease was likely due to the surface composition of Ru SAs-CoO_x partially transforming into amorphous species. In addition, inductively coupled plasma mass spectrometry (ICP-MS) was used to monitor the catalyst dissolution rate during chronopotentiometry tests at 10 mA cm^{-2} in 0.1 M $HClO_4$ solution. The results, as indicated in Table S7,† revealed very low rates of Ru and Co dissociation.

Owing to its excellent OER activity, an acidic electrolyzer was assembled using Ru SAs-CoO_x as the anode and commercial Pt/C as the cathode. As shown in Fig. 4f, the Pt/C//Ru SAs-CoO_x couple required only 1.44 V to achieve a current density of 10 mA cm^{-2}, lower than that of the Pt/C//RuO_2 couple (1.57 V at 10

mA cm^{-2}) and Pt/C//Co_3O_4 couple (1.70 V at 10 mA cm^{-2}). To sum up, compared with pristine Co_3O_4 and RuO_2, Ru SAs-CoO_x exhibited overwhelming advantages for the OER from the aspects of overpotential, Tafel slope, durability, water splitting, and C_{dl} (Fig. 4g).

Understanding the reaction mechanism

To rationalize the enhanced OER activity and durability of Ru SAs-CoO_x, the reaction mechanism was explored. *In situ* ^{18}O isotope labeling DEMS was used to validate the participation of the LOM during the OER process (Fig. 5a and b). The signals for the mass-to-charge ratio (m/z) = 34 were detected in gas production, which included the ^{18}O in the lattice and ^{16}O in the water,[67] confirming the successful ^{18}O labeling and the involvement of the LOM during the OER process (Fig. S35†).[34,68] In contrast, the signals of $^{34}O_2$ for pristine Co_3O_4 were not detected, demonstrating that the low Co–O covalency and less O_v concentration of Co_3O_4 would inhibit the LOM process. Therefore, the DEMS measurement confirmed the doping of Ru to be the switch for the transformation of the OER mechanism from the conventional AEM to the LOM.

To unveil the local environment and understand the reaction mechanisms of Ru SAs-CoO_x during the OER process, *in situ* Raman spectroscopy was performed as well. Fig. 5c exhibits the Raman spectra of Ru SAs-CoO_x recorded from 0 to 60 min at 1.5 V. Three characteristic peaks corresponding to the E_g (~465 cm^{-1}), F_{2g} (~505 cm^{-1}), and A_{1g} (~660 cm^{-1}) of Co_3O_4 spinel oxides were detected. With the increase in the OER time, a new

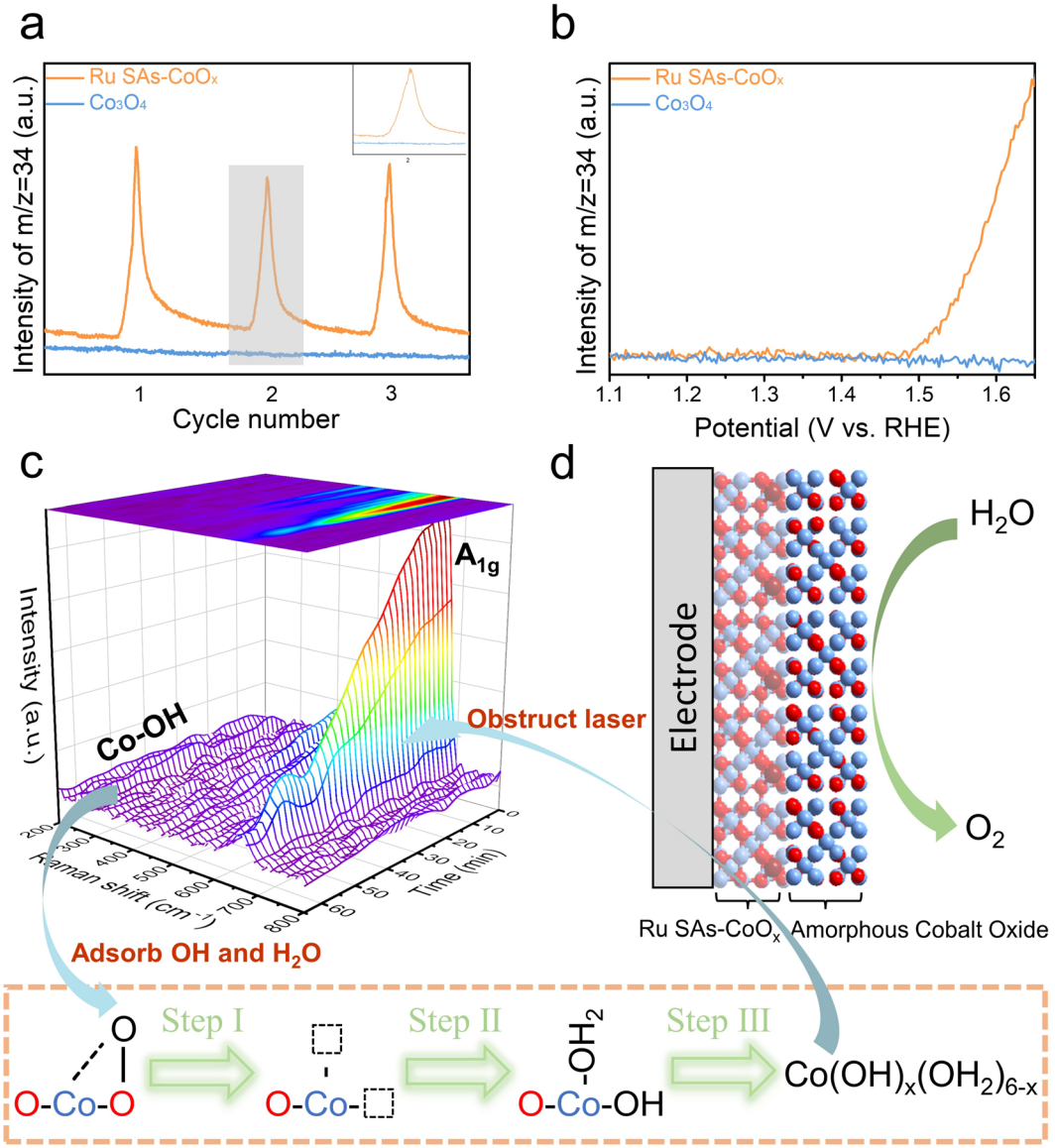

Fig. 5 Mechanism investigation of Ru SAs-CoO_x during the OER process. (a) *In situ* DEMS signals of $^{34}O_2$ for ^{18}O-labeled Ru SAs-CoO_x and Co_3O_4 in 0.1 M $HClO_4$ relative to time. (b) *In situ* DEMS signals of $^{34}O_2$ for ^{18}O-labeled Ru SAs-CoO_x and Co_3O_4 in 0.1 M $HClO_4$ relative to potential. (c) *In situ* Raman spectra recorded from 0 to 60 min. (d) Schematic diagram showing the electrochemical environment of Ru SAs-CoO_x during the OER process.

signal corresponding to the chemical bonds between adsorbed OH and Co atoms in the octahedral Co–OH gradually emerged at ~250 cm^{-1} (Fig. S36†),[69,70] suggesting the formation of amorphous Co–OH due to the existence of interim oxygen vacancies during consecutive vacancy filling/lattice oxygen migration in the LOM cycles. Thus, these vacancies could be easily occupied by OH and H_2O to form $Co(OH)_x(H_2O)_{6-x}$, which would slowly degrade into amorphous cobalt oxide. As a result, the intensity of all the peaks decreased substantially, and the full width at half maximum (FWHM) peak shape was also broadened because the growth of amorphous cobalt oxide obstructed the focal point of the laser.[19,71] Based on the above results, although the durability was maintained well during the OER process, the surface structure of Ru SAs-CoO_x during the OER process has gradually transformed into an amorphous cobalt oxide layer (Fig. 5d).

DFT calculations were also carried out to shed light on the enhanced catalytic performance of Ru SAs-CoO_x. The related models are constructed based on the experimental analysis. Then the Gibbs free energy of the elementary steps during the OER process is calculated, respectively. First, the traditional AEM pathway is considered for pristine Co_3O_4 and Ru SAs-CoO_x. Since vacancy filling/lattice oxygen migration is not involved in the AEM pathway, the oxygen vacancies are pre-created in the established model (Fig. S37–S39†). As shown in Fig. S40,† for the DFT results of the AEM pathway, the Co and Ru sites display a much higherenergy barrier than that of the Co site on pristine Co_3O_4. This finding contradicts the observed enhanced catalyticactivity of Ru SAs-CoO_x compared to that of pristine Co_3O_4. Then, the Gibbs free energy based on the LOM pathway was calculated. In this pathway, the oxygen vacancies are not pre-created in the established models because vacancy filling/lattice oxygen migration is involved in the LOM process. As exhibited in Fig. 6a–b and S41–S42,† the Ru site on Ru SAs-CoO_x cannot be an effective adsorption/desorption site for the LOM process owing to its too strong interaction with O*. In contrast, on the Co site, the largest change in free energy (not referred to as a potential-determining step due to step 4 being a chemical process without any charge transfer) is the formation of O_2 (step 4) and the corresponding free energy is 0.62 eV, significantly smaller than that of the AEM pathway without (1.04 eV)/with (1.42 eV) oxygen vacancies. It can be observed that the largest change in free energy of Ru SAs-CoO_x during the OER process is the formation of O_2, which is a chemical step without any charge transfer (Fig. S43–S44†). This finding was consistent with the Tafel slope analysis and suggested the presence of a mixed kinetic control mechanism.[52,54] Furthermore, an advanced activity descriptor $G_{max}(\eta)$ was also utilized to comprehensively evaluate their activity trends. This descriptor identifies the largest free-energy span (uphill in free energy) among all intermediates within the catalytic process, considering both the electrochemical and chemical steps.[72,73] As shown in Fig. S44,† when $U = 1.23$ V, the corresponding G_{max} for the LOM process (1.24 eV) is close to (less than 0.2 eV different from each other) that of the AEM process without oxygen vacancies (1.10 eV), while being smaller than that of the AEM process with oxygen vacancies (1.96 eV). Therefore, according to these above theoretical results, we assume that the LOM mechanism is operational during the OER process on Ru SAs-CoO_x. However, the actual OER process is complex, so the triggering of the LOM process does not imply the elimination of the AEM process. The enhanced catalytic activity contributed to the synergistic effect of AEM and LOM. Considering that a small portion of Ru was substituted for the O_h site of Co_3O_4, the free energy diagrams for the OER on the Co and Ru site of Ru SAs-CoO_x (with Ru replacing O_h sites) based on the LOM were also calculated. The results showed that on the model of Ru SAs-CoO_x (with Ru replacing O_h sites), both the Ru (1.13 eV) and Co sites (1.33 eV) displayed a much higher energy barrier than the Co site of Ru SAs-CoO_x (with Ru replacing T_d sites). Therefore, the Co and Ru site of Ru SAs-CoO_x (with Ru replacing O_h sites) cannot be the effective adsorption/desorption site for the LOM process (Fig. S45–S47†).

In addition, considering that the OH* coverage on the catalyst surface in acidic media is comparatively low, the energy barrier for the H_2O-dissociation is calculated to offer a side reflection of OH* formation and coverage.[74] As shown in Fig. 6c and S48–S50,† the Co site on Ru SAs-CoO_x displays a much lower energy barrier (0.53 eV) for H_2O-dissociation compared to that of pristine Co_3O_4 (0.61 eV) as the Ru site improves the H_2O-dissociation ability on the Co site nearby and provides more OH* species for the lattice oxygen oxidation. Therefore, although Ru centers cannot be the effective adsorption/desorption site for OER processes, the significance of Ru should not be disregarded. Specifically, the active sites should be derived from the "Ru–O–Co" structural unit (Co: optimal adsorption/desorption sites. Ru: improve the H_2O-dissociation ability on the lattice oxygen site and provide plentiful OH* species for the subsequent oxidation process; increase the Co–O covalency and facilitate the direct O–O coupling. O: directly involved in O_2 evolution).

Additionally, an acknowledged drawback that DFT computations have limitations in describing the surface structure must be pointed out. In this study, only the (311) facet of Co_3O_4 was selected as the model, which simplified the complex structure of the Ru SAs-CoO_x electrocatalyst. In addition, the surface structure of the catalyst has changed during the OER process. However, the DFT simulations here still provide a wide understanding of why the electrocatalytic activity of Ru SAs-CoO_x improved compared with that of Co_3O_4.

To understand the enhanced durability of the prepared Ru SAs-CoO_x, the following two aspects were discussed. (1) Static durability: as displayed in Fig. 6d, the Co vacancy formation energy of T_d and O_h sites at Ru SAs-CoO_x (T_d: 0.80 eV and O_h: 2.43 eV) is higher than that of pristine Co_3O_4 (T_d: 0.11 eV and O_h: 2.18 eV), indicating a thermodynamically less favorable dissolution of Co from Ru SAs-CoO_x. Here, the Co vacancy formation energy is calculated at 0 k in a vacuum environment. The real experimental environment involves factors such as temperature, voltage, solvent, *etc.*, which makes it easier to produce vacancies in the actual environment. Therefore, although the DFT results indicate that Co vacancy formation energy of Ru SAs-CoO_x and pristine Co_3O_4 is not thermodynamically favorable (formation energy > 0), it can be inferred

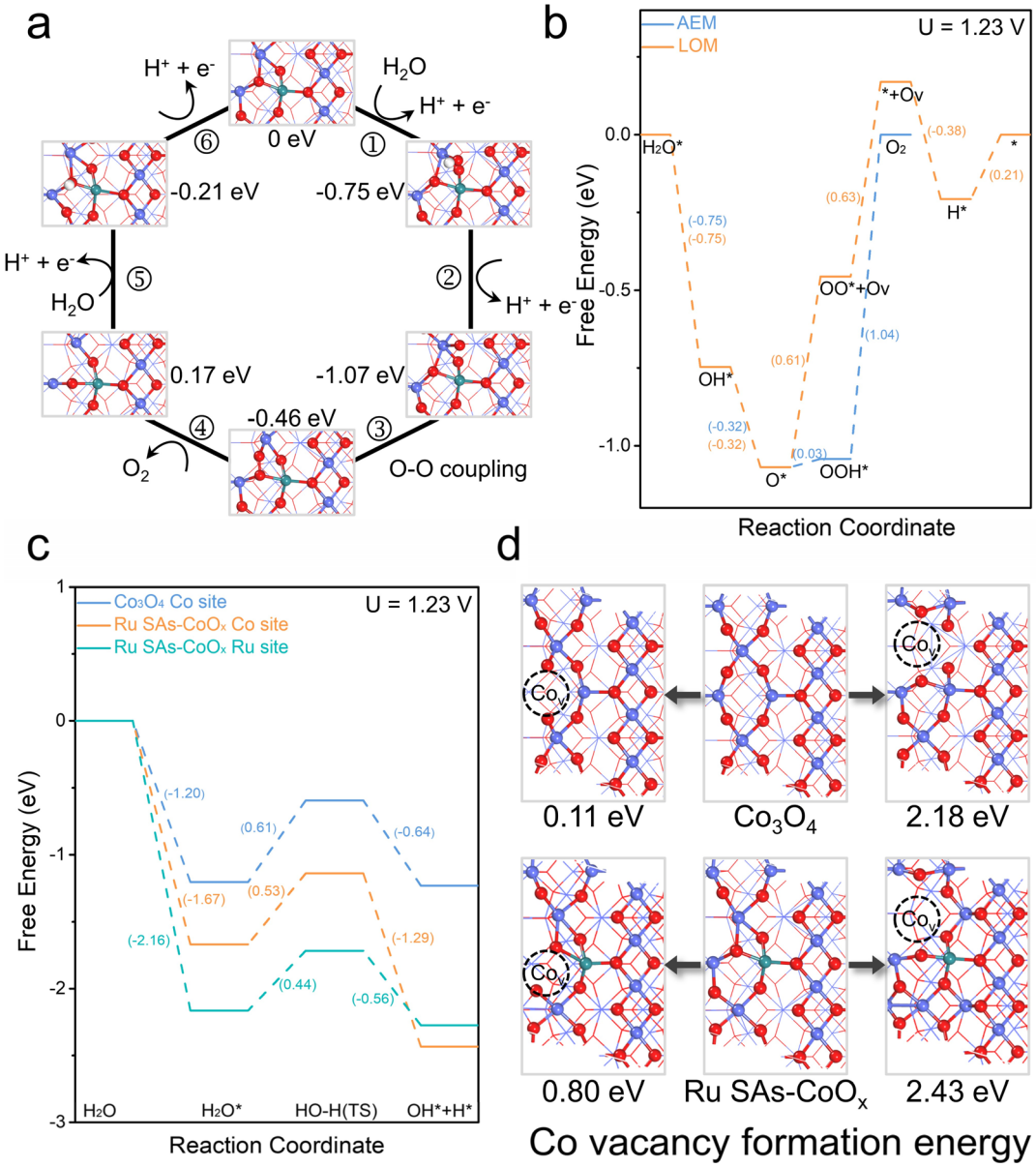

Fig. 6 Theoretical investigations. (a) Schematic illustration of the proposed OER mechanism based on the LOM process. (b) Calculated free energy diagrams for the OER on the Co site of Ru SAs-CoO_x (without oxygen vacancies) based on the AEM (corresponding to Fig. S34†) and LOM. (c) Calculated free energy diagram for H_2O-adsorption and H_2O-dissociation on different active sites. (d) Calculated Co vacancy formation energy on Co_3O_4 and Ru SAs-CoO_x.

from the trend of formation energy that the introduction of Ru enhances the static durability of Co. (2) Dynamic durability: direct O–O coupling mitigates the unstable reconstruction process before the formation of the OO bond, thereby extending the working lifetime of the electrocatalyst.

Conclusion

In this work, we reported a Ru SAs-CoO_x catalyst to overcome the balance between catalytic activity and dynamic durability for acidic OER *via* the preferential substitution of Ru for the Co^{2+} (T_d) site of Co_3O_4. Consequently, the overpotential at 10 mA cm^{-2} of as-prepared Co_3O_4 (395 mV) sharply decreases to 188 mV by doping a small amount of Ru atoms (5.16 wt%), and its long-term durability is also prolonged. Combined with *in situ* measurement and DFT calculation, we hypothesized that the boosted activity and durability originated from the enhanced OH* coverage and Co–O covalency of Co_3O_4 after the introduction of Ru, which provided more OH* species for the OER process and mitigated the unstable reconstruction process. In addition, the obtained Ru SAs-CoO_x is superior to commercial RuO_2 and IrO_2 in price (1/3 of RuO_2 and 1/15 of IrO_2, respectively). We believe these findings will not only provide a guideline for the design of more efficient and stable catalysts but also pave a new avenue for the further exploration of the active site structure and catalytic mechanisms.

Data availability

The data supporting this article have been included as part of the ESI.†

Author contributions

J. Z., X. F., and H. S. conceived the project. J. Z. performed the experiments. G. C., D. S., Y. T. and W. X. offered help to analyze and discuss the experiment data. J. Z. wrote the manuscript. G. C., X. F., and H. S. gave helpful advice on the manuscript preparation. X. F. and H. S. co-supervised the project. All authors have approved the final version of the manuscript.

Conflicts of interest

There are no conflicts to declare.

Acknowledgements

We acknowledge financial support from the Development Program of China (2021YFA1502700), the National Natural Science Foundation of China (22232004, 22209076 and 22279062), the National Key Research and, the Natural Science Foundation of Jiangsu Province (Grant No. BK 20220369), the European Union's Horizon 2020 research, innovation programme (GrapheneCore3: 881603), Deutsche Forschungsgemeinschaft within the Cluster of Excellence, and CRC 1415 (Grant No. 417590517). H. S is thankful for the financial support from Jiangsu Specially Appointed Professorship.

References

1 H. N. Nong, L. J. Falling, A. Bergmann, M. Klingenhof, H. P. Tran, C. Spöri, R. Mom, J. Timoshenko, G. Zichittella, A. Knop-Gericke, S. Piccinin, J. Pérez-Ramírez, B. R. Cuenya, R. Schlögl, P. Strasser, D. Teschner and T. E. Jones, *Nature*, 2020, **587**, 408–413.
2 X. Wang, S. Xi, P. Huang, Y. Du, H. Zhong, Q. Wang, A. Borgna, Y. Zhang, Z. Wang, H. Wang, Z. G. Yu, W. S. V. Lee and J. Xue, *Nature*, 2022, **611**, 702–708.
3 P. Zhai, M. Xia, Y. Wu, G. Zhang, J. Gao, B. Zhang, S. Cao, Y. Zhang, Z. Li, Z. Fan, C. Wang, X. Zhang, J. T. Miller, L. Sun and J. Hou, *Nat. Commun.*, 2021, **12**, 4587.
4 D. H. Kweon, M. S. Okyay, S.-J. Kim, J.-P. Jeon, H.-J. Noh, N. Park, J. Mahmood and J.-B. Baek, *Nat. Commun.*, 2020, **11**, 1278.
5 Y. Pan, X. Xu, Y. Zhong, L. Ge, Y. Chen, J.-P. M. Veder, D. Guan, R. O'Hayre, M. Li, G. Wang, H. Wang, W. Zhou and Z. Shao, *Nat. Commun.*, 2020, **11**, 2002.
6 K. Wang, Y. Wang, B. Yang, Z. Li, X. Qin, Q. Zhang, L. Lei, M. Qiu, G. Wu and Y. Hou, *Energy Environ. Sci.*, 2022, **15**, 2356–2365.
7 C.-Z. Yuan, S. Wang, K. San Hui, K. Wang, J. Li, H. Gao, C. Zha, X. Zhang, D. A. Dinh, X.-L. Wu, Z. Tang, J. Wan, Z. Shao and K. N. Hui, *ACS Catal.*, 2023, **13**, 2462–2471.
8 Y. Lin, Y. Dong, X. Wang and L. Chen, *Adv. Mater.*, 2023, **35**, 2210565.
9 H. Jin, X. Liu, P. An, C. Tang, H. Yu, Q. Zhang, H.-J. Peng, L. Gu, Y. Zheng, T. Song, K. Davey, U. Paik, J. Dong and S.-Z. Qiao, *Nat. Commun.*, 2023, **14**, 354.
10 M. F. Lagadec and A. Grimaud, *Nat. Mater.*, 2020, **19**, 1140–1150.
11 L. Li, P. Wang, Q. Shao and X. Huang, *Adv. Mater.*, 2021, **33**, 2004243.
12 Y. Wang, R. Yang, Y. Ding, B. Zhang, H. Li, B. Bai, M. Li, Y. Cui, J. Xiao and Z.-S. Wu, *Nat. Commun.*, 2023, **14**, 1412.
13 J. Kim, P. C. Shih, K. C. Tsao, Y. T. Pan, X. Yin, C. J. Sun and H. Yang, *J. Am. Chem. Soc.*, 2017, **139**, 12076–12083.
14 Y. Qin, T. Yu, S. Deng, X. Y. Zhou, D. Lin, Q. Zhang, Z. Jin, D. Zhang, Y. B. He, H. J. Qiu, L. He, F. Kang, K. Li and T. Y. Zhang, *Nat. Commun.*, 2022, **13**, 3784.
15 Y. Lin, Z. Tian, L. Zhang, J. Ma, Z. Jiang, B. J. Deibert, R. Ge and L. Chen, *Nat. Commun.*, 2019, **10**, 162.
16 X. Liang, L. Shi, Y. Liu, H. Chen, R. Si, W. Yan, Q. Zhang, G. D. Li, L. Yang and X. Zou, *Angew. Chem., Int. Ed.*, 2019, **58**, 7631–7635.
17 R. Zhang, N. Dubouis, M. Ben Osman, W. Yin, M. T. Sougrati, D. A. D. Corte, D. Giaume and A. Grimaud, *Angew. Chem., Int. Ed.*, 2019, **58**, 4571–4575.
18 I. C. Man, H.-Y. Su, F. Calle-Vallejo, H. A. Hansen, J. I. Martínez, N. G. Inoglu, J. Kitchin, T. F. Jaramillo, J. K. Nørskov and J. Rossmeisl, *ChemCatChem*, 2011, **3**, 1159–1165.
19 K. Natarajan, E. Munirathinam and T. C. K. Yang, *ACS Appl. Mater. Interfaces*, 2021, **13**, 27140–27148.
20 J. Huang, H. Sheng, R. D. Ross, J. Han, X. Wang, B. Song and S. Jin, *Nat. Commun.*, 2021, **12**, 3036.
21 Z. Liu, G. Wang, X. Zhu, Y. Wang, Y. Zou, S. Zang and S. Wang, *Angew. Chem., Int. Ed.*, 2020, **59**, 4736–4742.
22 N. Wang, P. Ou, R. K. Miao, Y. Chang, Z. Wang, S.-F. Hung, J. Abed, A. Ozden, H.-Y. Chen, H.-L. Wu, J. E. Huang, D. Zhou, W. Ni, L. Fan, Y. Yan, T. Peng, D. Sinton, Y. Liu, H. Liang and E. H. Sargent, *J. Am. Chem. Soc.*, 2023, **145**, 7829–7836.
23 F.-Y. Chen, Z.-Y. Wu, Z. Adler and H. Wang, *Joule*, 2021, **5**, 1704–1731.
24 X. Wang, H. Zhong, S. Xi, W. S. V. Lee and J. Xue, *Adv. Mater.*, 2022, **34**, 2107956.
25 L. Li, P. Wang, Q. Shao and X. Huang, *Adv. Mater.*, 2021, **33**, 2004243.
26 J. Rossmeisl, Z. W. Qu, H. Zhu, G. J. Kroes and J. K. Nørskov, *J. Electroanal. Chem.*, 2007, **607**, 83–89.
27 A. Grimaud, O. Diaz-Morales, B. Han, W. T. Hong, Y.-L. Lee, L. Giordano, K. A. Stoerzinger, M. T. M. Koper and Y. Shao-Horn, *Nat. Chem.*, 2017, **9**, 457–465.
28 Z.-F. Huang, J. Song, Y. Du, S. Xi, S. Dou, J. M. V. Nsanzimana, C. Wang, Z. J. Xu and X. Wang, *Nat. Energy*, 2019, **4**, 329–338.
29 J. Hwang, R. R. Rao, L. Giordano, Y. Katayama, Y. Yu and Y. Shao-Horn, *Science*, 2017, **358**, 751–756.
30 E. Fabbri and T. J. Schmidt, *ACS Catal.*, 2018, **8**, 9765–9774.

31 Z. Shi, J. Li, Y. Wang, S. Liu, J. Zhu, J. Yang, X. Wang, J. Ni, Z. Jiang, L. Zhang, Y. Wang, C. Liu, W. Xing and J. Ge, *Nat. Commun.*, 2023, **14**, 843.
32 A. Grimaud, A. Demortière, M. Saubanère, W. Dachraoui, M. Duchamp, M.-L. Doublet and J.-M. Tarascon, *Nat. Energy*, 2016, **2**, 16189.
33 H. Shin, H. Xiao and W. A. Goddard III, *J. Am. Chem. Soc.*, 2018, **140**, 6745–6748.
34 A. Grimaud, O. Diaz-Morales, B. Han, W. T. Hong, Y. L. Lee, L. Giordano, K. A. Stoerzinger, M. T. M. Koper and Y. Shao-Horn, *Nat. Chem.*, 2017, **9**, 457–465.
35 J. B. Goodenough, *Chem. Mater.*, 2014, **26**, 820–829.
36 J. Kim, C.-W. Roh, S. K. Sahoo, S. Yang, J. Bae, J. W. Han and H. Lee, *Adv. Energy Mater.*, 2018, **8**, 1701476.
37 J. Zhang, G. Chen, Q. Liu, C. Fan, D. Sun, Y. Tang, H. Sun and X. Feng, *Angew. Chem., Int. Ed.*, 2022, **61**, e202209486.
38 Q. He, D. Tian, H. Jiang, D. Cao, S. Wei, D. Liu, P. Song, Y. Lin and L. Song, *Adv. Mater.*, 2020, **32**, e1906972.
39 C. Geng, D. Rathore, D. Heino, N. Zhang, I. Hamam, N. Zaker, G. A. Botton, R. Omessi, N. Phattharasupakun, T. Bond, C. Yang and J. R. Dahn, *Adv. Energy Mater.*, 2022, **12**, 2103067.
40 M. Moses-DeBusk, M. Yoon, L. F. Allard, D. R. Mullins, Z. Wu, X. Yang, G. Veith, G. M. Stocks and C. K. Narula, *J. Am. Chem. Soc.*, 2013, **135**, 12634–12645.
41 S. Yang, J. Kim, Y. J. Tak, A. Soon and H. Lee, *Angew. Chem., Int. Ed.*, 2016, **55**, 2058–2062.
42 B. Qiao, A. Wang, X. Yang, L. F. Allard, Z. Jiang, Y. Cui, J. Liu, J. Li and T. Zhang, *Nat. Chem.*, 2011, **3**, 634–641.
43 J. B. Pan, B. H. Wang, J. B. Wang, H. Z. Ding, W. Zhou, X. Liu, J. R. Zhang, S. Shen, J. K. Guo, L. Chen, C. T. Au, L. L. Jiang and S. F. Yin, *Angew. Chem., Int. Ed.*, 2021, **60**, 1433–1440.
44 Z. Xiao, Y. Wang, Y.-C. Huang, Z. Wei, C.-L. Dong, J. Ma, S. Shen, Y. Li and S. Wang, *Energy Environ. Sci.*, 2017, **10**, 2563–2569.
45 L. Xu, Q. Jiang, Z. Xiao, X. Li, J. Huo, S. Wang and L. Dai, *Angew. Chem., Int. Ed.*, 2016, **55**, 5277–5281.
46 B. Guo, R. Ma, Z. Li, J. Luo, M. Yang and J. Wang, *Mater. Chem. Front.*, 2020, **4**, 1390–1396.
47 W. I. Choi, S. Choi, M. Balamurugan, S. Park, K. H. Cho, H. Seo, H. Ha and K. T. Nam, *ACS Omega*, 2023, **8**, 35034–35043.
48 P. Li, M. Wang, X. Duan, L. Zheng, X. Cheng, Y. Zhang, Y. Kuang, Y. Li, Q. Ma, Z. Feng, W. Liu and X. Sun, *Nat. Commun.*, 2019, **10**, 1711.
49 J. Shan, C. Ye, S. Chen, T. Sun, Y. Jiao, L. Liu, C. Zhu, L. Song, Y. Han, M. Jaroniec, Y. Zhu, Y. Zheng and S.-Z. Qiao, *J. Am. Chem. Soc.*, 2021, **143**, 5201–5211.
50 Z. Zhang, C. Feng, D. Wang, S. Zhou, R. Wang, S. Hu, H. Li, M. Zuo, Y. Kong, J. Bao and J. Zeng, *Nat. Commun.*, 2022, **13**, 2473.
51 Y. Xue, J. Fang, X. Wang, Z. Xu, Y. Zhang, Q. Lv, M. Liu, W. Zhu and Z. Zhuang, *Adv. Funct. Mater.*, 2021, **31**, 2101405.
52 E. Tsuji, A. Imanishi, K.-i. Fukui and Y. Nakato, *Electrochim. Acta*, 2011, **56**, 2009–2016.
53 L. A. De Faria, J. F. C. Boodts and S. Trasatti, *J. Appl. Electrochem.*, 1996, **26**, 1195–1199.
54 J. O. M. Bockris, *J. Chem. Phys.*, 1956, **24**, 817–827.
55 J. Shan, T. Ling, K. Davey, Y. Zheng and S.-Z. Qiao, *Adv. Mater.*, 2019, **31**, 1900510.
56 J. Shan, C. Guo, Y. Zhu, S. Chen, L. Song, M. Jaroniec, Y. Zheng and S.-Z. Qiao, *Chem*, 2019, **5**, 445–459.
57 G. Wu, X. Zheng, P. Cui, H. Jiang, X. Wang, Y. Qu, W. Chen, Y. Lin, H. Li, X. Han, Y. Hu, P. Liu, Q. Zhang, J. Ge, Y. Yao, R. Sun, Y. Wu, L. Gu, X. Hong and Y. Li, *Nat. Commun.*, 2019, **10**, 4855.
58 O. Diaz-Morales, S. Raaijman, R. Kortlever, P. J. Kooyman, T. Wezendonk, J. Gascon, W. T. Fu and M. T. M. Koper, *Nat. Commun.*, 2016, **7**, 12363.
59 X. Liang, L. Shi, Y. Liu, H. Chen, R. Si, W. Yan, Q. Zhang, G.-D. Li, L. Yang and X. Zou, *Angew. Chem., Int. Ed.*, 2019, **58**, 7631–7635.
60 X. Cui, P. Ren, C. Ma, J. Zhao, R. Chen, S. Chen, N. P. Rajan, H. Li, L. Yu, Z. Tian and D. Deng, *Adv. Mater.*, 2020, **32**, 1908126.
61 Y. L. Wu, X. Li, Y. S. Wei, Z. Fu, W. Wei, X. T. Wu, Q. L. Zhu and Q. Xu, *Adv. Mater.*, 2021, **33**, e2006965.
62 L. Trotochaud, J. K. Ranney, K. N. Williams and S. W. Boettcher, *J. Am. Chem. Soc.*, 2012, **134**, 17253–17261.
63 M. S. Burke, M. G. Kast, L. Trotochaud, A. M. Smith and S. W. Boettcher, *J. Am. Chem. Soc.*, 2015, **137**, 3638–3648.
64 M. B. Stevens, L. J. Enman, A. S. Batchellor, M. R. Cosby, A. E. Vise, C. D. M. Trang and S. W. Boettcher, *Chem. Mater.*, 2017, **29**, 120–140.
65 M. Favaro, J. Yang, S. Nappini, E. Magnano, F. M. Toma, E. J. Crumlin, J. Yano and I. D. Sharp, *J. Am. Chem. Soc.*, 2017, **139**, 8960–8970.
66 Y. Zhu, J. Wang, T. Koketsu, M. Kroschel, J. M. Chen, S. Y. Hsu, G. Henkelman, Z. Hu, P. Strasser and J. Ma, *Nat. Commun.*, 2022, **13**, 7754.
67 Y. Wen, P. Chen, L. Wang, S. Li, Z. Wang, J. Abed, X. Mao, Y. Min, C. T. Dinh, P. D. Luna, R. Huang, L. Zhang, L. Wang, L. Wang, R. J. Nielsen, H. Li, T. Zhuang, C. Ke, O. Voznyy, Y. Hu, Y. Li, W. A. Goddard Iii, B. Zhang, H. Peng and E. H. Sargent, *J. Am. Chem. Soc.*, 2021, **143**, 6482–6490.
68 Z. Shi, Y. Wang, J. Li, X. Wang, Y. Wang, Y. Li, W. Xu, Z. Jiang, C. Liu, W. Xing and J. Ge, *Joule*, 2021, **5**, 2164–2176.
69 R. Zhang, L. Pan, B. Guo, Z. F. Huang, Z. Chen, L. Wang, X. Zhang, Z. Guo, W. Xu, K. P. Loh and J. J. Zou, *J. Am. Chem. Soc.*, 2023, **145**, 2271–2281.
70 S. R. Shieh and T. S. Duffy, *Phys. Rev. B*, 2002, **66**, 134301.
71 C. Pasquini, L. D'Amario, I. Zaharieva and H. Dau, *J. Chem. Phys.*, 2020, **152**, 194202.
72 K. S. Exner, *ACS Catal.*, 2020, **10**, 12607–12617.
73 S. Razzaq and K. S. Exner, *ACS Catal.*, 2023, **13**, 1740–1758.
74 J. Yin, J. Jin, M. Lu, B. Huang, H. Zhang, Y. Peng, P. Xi and C.-H. Yan, *J. Am. Chem. Soc.*, 2020, **142**, 18378–18386.